

# Three-dimensional transverse instabilities in detached boundary layers

By FRANÇOIS GALLAIRE<sup>1</sup>, MATTHIEU MARQUILLIE<sup>2</sup>  
AND UWE EHRENSTEIN<sup>1</sup>

<sup>1</sup>Laboratoire J. A. Dieudonné, Université de Nice-Sophia Antipolis,  
Parc Valrose, F-06108 Nice Cedex 02, France

<sup>2</sup>Laboratoire de Mécanique de Lille, Université des Sciences et Technologies de Lille,  
Boulevard Paul Langevin, F-59655 Villeneuve d'Ascq Cédex, France

(Received 13 June 2005 and in revised form 12 July 2006)

A direct numerical simulation of the incompressible Navier–Stokes equations of the flow over a bump shows a stationary longitudinal instability at a Reynolds number of  $Re = 400$ . A three-dimensional global mode linear analysis is used to interpret these results and shows that the most unstable eigenmode is steady and localized in the recirculation bubble, with spanwise wavelength of approximately ten bump heights. An inviscid geometrical optics analysis along closed streamlines is then proposed and modified to account for viscous effects. This motivates a final discussion regarding the physical origin of the observed instability.

---

## 1. Introduction

Detached laminar boundary layers occur in many engineering applications and are known to induce efficiency losses, such as drag increase and lift loss on airfoils at high angles of attack. The initial approach followed in the study of the destabilization of laminar separating flows was restricted to a two-dimensional setting. For the archetypal flow over a backward facing step, oscillations are triggered beyond a certain critical Reynolds number  $Re_c$ . The physical mechanisms at the origin of these oscillations are only partially understood. Kaiktsis, Karniadakis & Orszag (1996) first suggested a noise amplifier behaviour, reminiscent of convective instabilities. The presence of a finite region of absolute instability was then thought to play a role in boundary layer flows with adverse pressure gradient (Hammond & Redekopp 1998). This interpretation has recently been corroborated by the study of Marquillie & Ehrenstein (2003) on laminar separated bubbles generated over various smooth bumps. However, the exact role of topological changes in the base flow structure as put forward by Theofilis, Hein & Dallmann (2000), which may even lead to the disappearance of the steady nonlinear global equilibrium state of the Navier–Stokes equations, is not understood.

Coming back to the flow over a backward facing step and allowing for three-dimensional flow development, the experiments by Armaly *et al.* (1983) and numerical simulations by Kaiktsis, Karniadakis & Orszag (1991) and more recently Williams & Baker (1997) concluded that there was a strong influence of sidewalls. In the absence of sidewalls the recent numerical stability analysis of Barkley, Gomes & Henderson (2002) as well as the experimental studies of Beaudoin *et al.* (2004) have revealed that a primary longitudinal steady instability first takes place when the Reynolds number

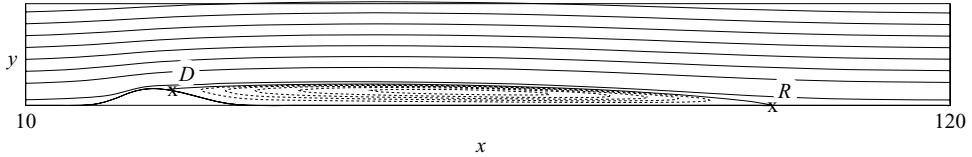


FIGURE 1. Streamlines of the two-dimensional base state at  $Re = 400$ .

exceeds a threshold Reynolds number  $Re_{3D}$  below  $Re_c$ . These authors have deduced from a qualitative inspection of the two-dimensional base state that the physical mechanism leading to the formation of these longitudinal structures is an instability of centrifugal type and they have identified the destabilizing regions of the flow.

The goal of the present study is to analyse this three-dimensional instability in the case of the flow over a bump sketched in figure 1, in the absence of sidewalls. The study combines three different approaches: a three-dimensional direct numerical simulation (DNS), a global stability analysis and an inviscid geometrical optics analysis along closed streamlines. This method, which was first developed for the study of the elliptic instability of vortices (Bayly 1986) and then applied to hyperbolic and centrifugal instabilities (Bayly 1988; Lifshitz & Hameiri 1991; Sipp & Jacquin 1998), is borrowed from the stability analysis of Euler nonlinear equilibrium states. Note that the numerical complexity decreases for each of these steps, the most prohibitive being the three-dimensional DNS, which has led us to limit the scope of the paper to a single bump geometry.

The outline of the paper is as follows: §2 is devoted to the two-dimensional base flow and three-dimensional numerical simulation. The results are then compared in §3 to a global mode stability analysis. In §4, we show that the physical mechanisms at the origin of this instability can be understood by considering the inviscid geometrical optics stability analysis along closed streamlines. A conclusion section closes the paper.

## 2. Direct numerical simulation

At the domain entrance at  $x=0$  a Blasius profile is imposed, non-dimensionalized such that the outer velocity at  $y=\infty$  is  $U=1$  and that the displacement thickness associated with the local Blasius boundary layer profile is  $\delta(x=0)=\delta_0=1$ . The bump geometry  $b(x)$  is given in Marquillie & Ehrenstein (2003): its height is taken to be  $h=2$  and the bump is located between  $x=15$  and  $x=37$  with the summit at  $x=25$ . The Reynolds number is taken as  $Re=U\delta_0/\nu=400$  ( $\nu$  being the kinematic viscosity) such that  $Re_{3D} < Re < Re_c$  ( $Re_c=600$  for the onset of oscillations according to Marquillie & Ehrenstein 2003). At this Reynolds number, a long recirculation zone develops that links the detachment point  $D$  at  $x \sim 28$  to the reattachment point  $R$  at  $x \sim 100$ . The bump and the recirculation zone are represented in figure 1.

The algorithm used is a generalization of the two-dimensional numerical simulation procedure detailed in Marquillie & Ehrenstein (2002). The bump geometry  $y=b(x)$  is taken into account by using an algebraic mapping onto a Cartesian grid. The three-dimensional Navier–Stokes equations are then discretized using fourth-order finite differences in the streamwise  $x$  direction with  $N_x=1024$  equidistant grid points for a domain length of  $L_x=200$ , whereas a pseudo-spectral Chebyshev collocation method is used in the normal  $y$ -direction with  $N_y=97$  covering the region  $[0, L_y=100]$  after a suitable coordinate transform from the Gauss–Lobatto points in  $[-\pi, \pi]$ . Along the transverse direction  $-L_z < z < L_z$ , the flow is assumed periodic of period  $2L_z$ ,

calling for a spectral Fourier expansion along the transverse coordinate with  $N_z = 64$  modes. The three-dimensional system largely uncouples into  $N_z$  two-dimensional subsystems analogous to the two-dimensional system studied in detail by Marquillie & Ehrenstein (2002), though nonlinear coupling terms linking the different Fourier modes appear. They involve convolution products which are classically evaluated in physical space using fast Fourier transforms (FFTs). The conventional de-aliasing technique with  $M \geq 3N_z/2$  effective transverse Fourier modes is used. This type of algorithm is suitable for parallelization, which has been implemented with up to 8 processors on the NEC SX5 at IDRIS (French National Computer Center), yielding a final 40 GFlops performance.

Second-order backward Euler differencing is used in time: the Cartesian part of the diffusion term is taken implicitly whereas the nonlinear and metric terms are evaluated using an explicit second-order Adams–Bashworth scheme. In order to ensure a divergence-free velocity field, a fractional step method is used, adding to each prediction step a suitable projection step.

As already mentioned, a Blasius profile is prescribed at the inlet, whereas at outflow the classical advection condition

$$\frac{\partial \mathbf{U}}{\partial t} + U_c \frac{\partial \mathbf{U}}{\partial x} = 0 \quad \text{with} \quad U_c = \frac{1}{y^*} \int_0^{y^*} u(L_x, y) dy \quad (2.1)$$

is taken. The upper bound  $y^*$  in the integral is time-dependent during the transient unsteady flow regime; its value is such that  $U(L_x, y^*) \sim 0.5$ . A no-slip boundary condition is imposed on the wall whereas at  $y = b(x) + 100$  mixed Dirichlet–Neuman boundary conditions have been retained:

$$\frac{\partial u}{\partial y} = 0, \quad v = 0, \quad w = 0. \quad (2.2)$$

We have not attempted a systematic study of the influence of the imposed transverse period nor to a precise determination of  $Re_{3D}$  for reasons related to the computational cost of these time-consuming three-dimensional unsteady Navier–Stokes computations.

The simulation is initiated with the two-dimensional equilibrium state, to which a small transverse perturbation is added. In the present example for  $L_z = \pi/0.125$ , the chosen box width allows the evolution of wavenumbers as low as  $\beta_1 = 0.125$  and its harmonics  $\beta_n = 0.125n$ . This  $L_z$  value has been inferred from the linear instability results to be discussed in §3. The initial Gaussian divergence-free perturbation of  $U$  and  $V$  consists of the superposition of modes 1 to 4 with equal maximal amplitudes of  $5 \times 10^{-4}$  on  $U$  and  $10^{-8}$  on  $V$ .

Since  $Re > Re_{3D}$ , the perturbation grows but the growth factors are so weak that saturation cannot be reached within a reasonable computational time. This evolution is monitored by decomposing the transverse velocity field into its Fourier components  $W(x, y, z) = \sum W_n(x, y) \sin(\beta_n z)$  and their amplitudes  $W_n = \max(|W_n(x, y)|)$ . Figure 2(a) displays the evolution of the  $W_n$ ,  $n = 1 \dots 5$ , on a logarithmic scale in the time interval  $1000 < t < 1400$ . The exponential growth of modes 1 to 4 as well the exponential decay of mode 5 are clearly shown, mode 2 displaying the highest growth rate. One may take advantage of the rigorous exponential growth and decay of the modes to extract growth rates that will be compared to their counterparts calculated by the global stability analysis results in §3.

The extremely slow development of the structure makes it nearly intractable within a reasonable computational time. A similar slowness has been encountered in the

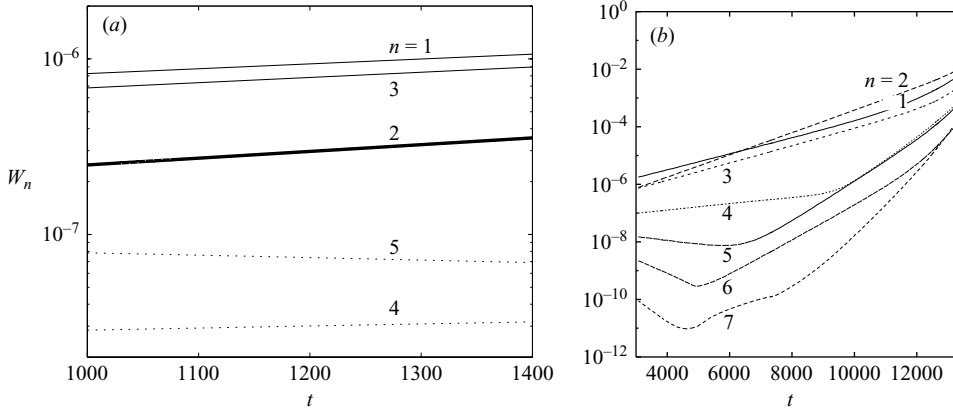


FIGURE 2. (a) Evolution of the maximum absolute transverse velocity  $W_n = \max(|W_n(x, y)|)$  for modes  $n = 1 \dots 5$  on a logarithmic scale between times  $t = 1000$  and  $t = 1400$ . These modes correspond to wavenumbers  $\beta_n = 0.125n$  and the growth rates extracted from this figure are reported in figure 4. (b) Evolution at later times  $t = 3000$  to  $t = 13000$  with only 16 Fourier modes. At time  $t = 14000$ , the effect of the spanwise truncation becomes important and erratic flow oscillations set in.

experiments of Beaudoin *et al.* (2004). Based on a linear extrapolation and on a simplified amplitude equation, we have estimated the time necessary for the most unstable mode  $\beta_2 = 0.25$  to dominate the flow ( $t = 6000$  approximately) as well as the time required for nonlinear terms to become significant ( $t = 10000$  approximately) and both are far beyond any reasonable computational effort, even on the fast NEC-SX5 computer at IDRIS. These estimations have been confirmed by running a similar DNS but truncating the Fourier expansion in the spanwise direction and keeping only 16 modes. This calculation, reported in figure 2(b), shows that the flow smoothly enters the nonlinear regime through the route predicted by the linear stability analysis. However, because of the setting in of erratic oscillations, no reasonable interpretation is possible beyond  $t = 13000$ . Indeed, in order to get reliable results for later times, one should significantly increase the Fourier expansion, which is beyond the scope of the present analysis.

Figure 3 represents the isocontours of the transverse component  $W(x, y, z)$  at time  $t = 1000$  at  $Re = 400$  and  $L_z = \pi/0.125$ . Figure 3(a) is an  $(x, z)$ -cut at  $y = 2$  and displays a structure resulting from the superposition of modes 1 to 4 displayed in figure 3(b–e). The use of the same grey scale on these four subfigures enables one to compare the relative amplitudes of the various modes in accordance with figure 2. Figure 3(f), which represents the flow structure of mode 2 in an  $(x, y)$ -cut at  $z = L_z/4$ , demonstrates that the structure is contained in the recirculation zone and has two amplitude peaks: one that is particularly intense in the vicinity of the detachment point  $D$  and another that spreads out in the downstream part of the recirculation zone.

### 3. Global modes

In order to interpret the formation of longitudinal structures in the flow, a global stability study is conducted. In contrast to local stability analyses where the stability of the base flow is analysed under the weakly non-parallel assumption, two-dimensional temporal eigenmodes are determined in the global stability setting, allowing for strong non-parallel base flows, such as the one encountered in the wake of the bump. The Navier–Stokes equations are linearized around the two-dimensional base state

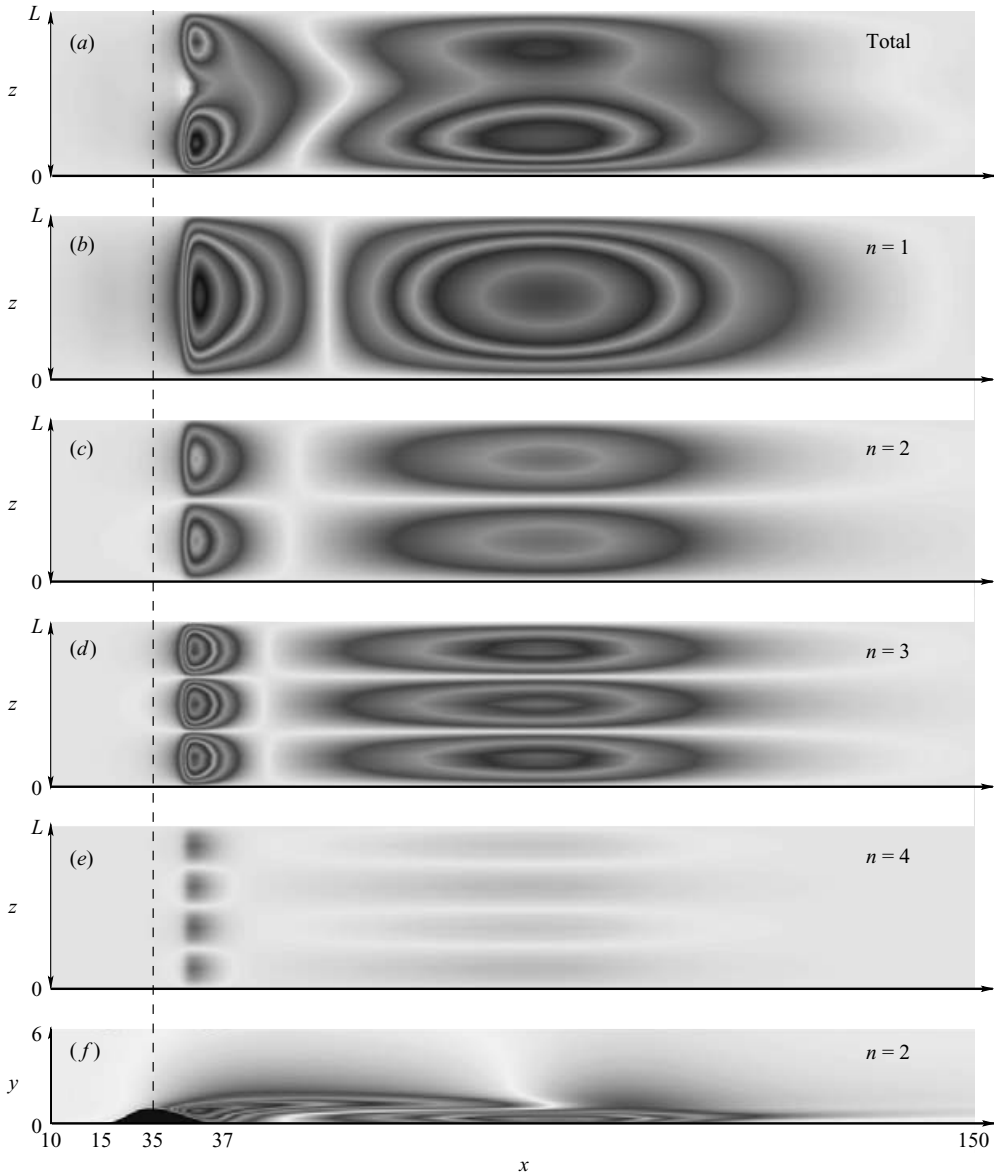


FIGURE 3. Transverse velocity component  $W(x, y, z)$  of the flow and its harmonic components at time  $t = 1000$ ,  $Re = 400$  for  $L_z = \pi/0.125$ : (a)  $(x, z)$ -cut at  $y = 2$ ; only half of the spanwise domain is shown, from 0 to  $L_z$ ; (b–e)  $(x, z)$ -cut at  $y = 2$  of its harmonic components  $W_n(x, y = 2)\sin(\beta_n z)$  (the same grey scale is used on (b–e) to ease comparison); (f) mode  $n = 2$  component  $W_2(x, y)$  in the  $(x, y)$ -plane at  $z = L_z/4$ .

$\mathbf{U} = (U(x, y), V(x, y), 0)$ , obtained numerically as a steady state of the simulation of the two-dimensional Navier–Stokes equations, and the three-dimensional flow perturbation is the solution of

$$\frac{\partial \mathbf{u}}{\partial t} = -(\mathbf{U} \cdot \nabla) \mathbf{u} - (\mathbf{u} \cdot \nabla) \mathbf{U} - \nabla p + \frac{1}{Re} \nabla^2 \mathbf{u}, \tag{3.1}$$

$$\nabla \cdot \mathbf{u} = 0, \tag{3.2}$$

where  $\mathbf{u} = (u, v, w)$  and  $p$  are the velocity and pressure perturbations. Equations (3.1) and (3.2) are solved for the temporal global two-dimensional modes

$$[\mathbf{u}(x, y, z, t), p(x, y, z, t)] = [\hat{\mathbf{u}}(x, y), \hat{p}(x, y)]e^{\sigma t + i\beta z} \quad (3.3)$$

with suitable boundary conditions for the three velocity components. Dirichlet boundary conditions are prescribed on the solid wall ( $y=b(x)$ ) and at infinity ( $y=y_{max}$ ), as well as at the inlet ( $x=0$ ). Neumann boundary conditions are imposed at the outlet ( $x=L$ ).

The type of discretization used to recover the base state by solving the Navier–Stokes equations is not suitable for solving the stability system since, as will become clear below, our strategy to determine the most unstable global modes requires the solution of linear systems involving the stability matrix of size  $4 \times N_x \times N_y$ . The base flow  $\mathbf{U}$  extracted from the 2D numerical simulation, as well as its derivatives, are therefore first interpolated onto a Chebyshev–Chebyshev collocation grid in the directions  $x$  and  $y$  with  $n_x = 160$  and  $n_y = 35$ , yielding a matrix approximately of size  $\sim 25\,000$ . We have checked that the significant eigenvalues do not change by more than 0.2% on increasing the resolution to  $n_x = 180$  and  $n_y = 45$ .

The pressure boundary conditions are given implicitly through the incompressibility condition which is imposed in the interior of the domain as well as on the boundary. Once the four corner points are eliminated, one obtains exactly the same number of unknowns as equations and is left with the following generalized eigenvalue problem after discretization:

$$\mathbf{A}\mathbf{v} = \sigma\mathbf{B}\mathbf{v}, \quad (3.4)$$

the vector  $\mathbf{v}$  containing the disturbance flow velocity and pressure. Despite the interpolation procedure, the generalized eigenvalue problem obtained after interpolation is still too large to be solved directly. A Krylov subspace projection method using a shift-and-invert strategy provides a way to recover the most significant eigenvalues (details may be found in Ehrenstein & Gallaire 2005). For each value of  $\beta$ , the calculation takes about 2 h CPU on the NEC/SX5 of IDRIS.

Figure 4, obtained upon repeating this procedure for various values of  $\beta$ , depicts the evolution of the maximum growth rate as a function of the wavenumber  $\beta$ . Note that in the present calculations, at most one unstable mode has been obtained, other modes being damped. In accordance with the three-dimensional numerical simulations, the structure is stationary ( $\sigma_i = 0$ ). Figure 4 also shows that the most unstable wavenumber at  $Re = 400$  is  $\beta_{max} = 0.25$  whereas the cut-off approximately equals  $\beta_c = 0.58$ . The growth rates extracted from the DNS, depicted by  $\times$ , are also plotted in figure 4 and compare very favourably with the global eigenvalues, justifying *a posteriori* the choice of  $L_z = \pi/0.125$  as suitable to sustain the highest possible growth at  $\beta_2 = 0.25$ . Figure 5 represents the most unstable mode structure at  $\beta_{max} = 0.25$ . The comparison with the snapshot of second harmonic  $W_2(x, y)$  at  $\beta_2 = 0.25$  displayed in figure 3(f) obtained by time evolution of the three-dimensional DNS in the preceding section is particularly striking.

#### 4. Local criteria

In this section, we tentatively apply the tools of the inviscid short-wave asymptotic stability analysis to the description of the instability developing, in the presence of viscosity, on a steady equilibrium state satisfying the Navier–Stokes equations. The

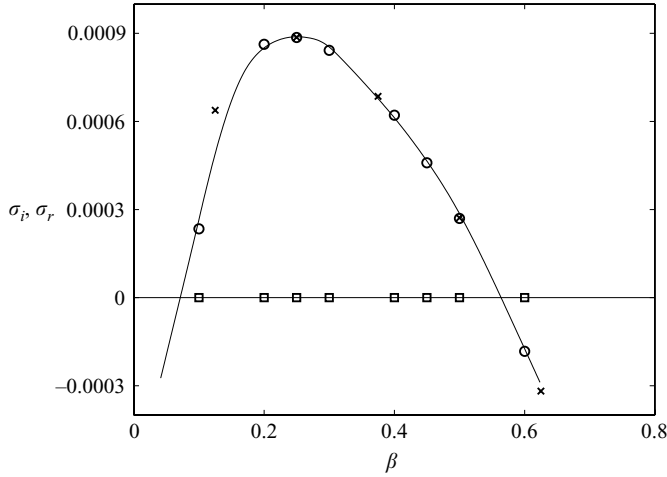


FIGURE 4. Growth rate ( $\circ$ ) and frequency ( $\square$ ) of the most unstable global mode as a function of the transverse wavenumber  $\beta$ . Growth rates extracted from the DNS are also shown ( $\times$ ).

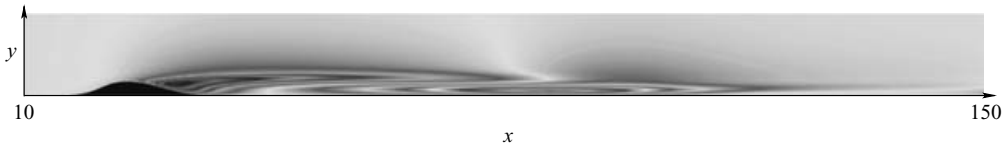


FIGURE 5. Transverse velocity component  $\hat{w}$  of the most unstable global mode at  $Re = 400$  corresponding to  $\beta_{max} = 0.25$ .

so-called geometric optics (or WKB) method is first recalled and applied to the closed streamlines in the recirculation bubble. *Ad hoc* terms accounting for the viscosity and finite wavenumber are then proposed in the next subsection. The viscosity introduces two main differences. First, the base flow is no longer a steady solution of the Euler equations and for instance the property that the vorticity remains constant on a streamline is not satisfied. Secondly, the viscosity plays a damping role in the perturbation amplitude evolution. Landman & Saffman (1987) have shown how to take into account this influence of the viscosity.

#### 4.1. Centrifugal instability mechanism

Sipp & Jacquin (2000) have derived a sufficient criterion for centrifugal instability in the inviscid and short-wave limit: the flow is unstable if there exists a streamline  $\psi_0$  such that for any point  $r_0$  belonging to the streamline the Rayleigh discriminant is negative, that is

$$\Delta(r_0) = 2|U|\Omega/\mathcal{R}(r_0) < 0, \quad (4.1)$$

over the whole streamline, where  $|U|$  is the velocity modulus,  $\Omega = \partial V/\partial x - \partial U/\partial y$  the vorticity and  $\mathcal{R}$  the local algebraic curvature radius

$$\mathcal{R} = \frac{|U|^3}{(\nabla\psi) \cdot [U \cdot \nabla U]}. \quad (4.2)$$

In expression (4.2) the usual streamfunction  $\psi$  has been introduced. In a way analogous to Beaudoin *et al.* (2004) but in contrast to Barkley *et al.* (2002), here the local Rayleigh discriminant is calculated using the local curvature radius  $\mathcal{R}$  and

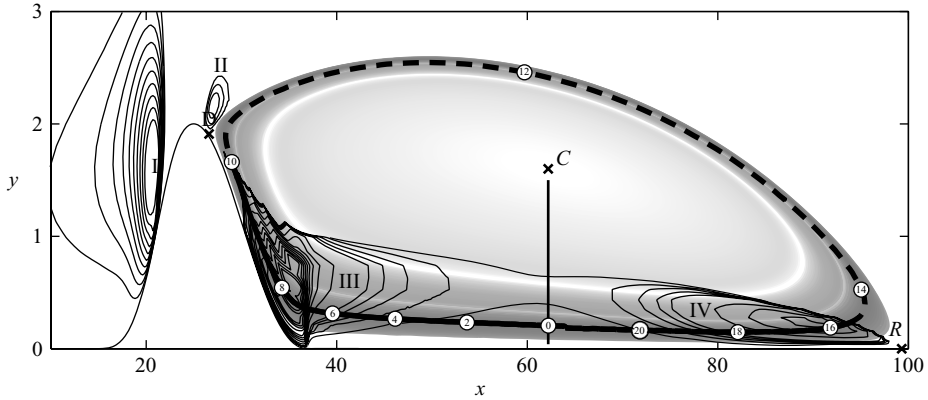


FIGURE 6. Isovalues of the growth rate predicted by WKB analysis along the streamlines are represented in grey levels. The most unstable streamline is represented by a dashed line and the time instants, with  $t_i = i \times 100$ ,  $i = 0, 2, \dots, 20$  at which the various points on the streamline are attained are indexed by their circled value. Isocontours of the Rayleigh discriminant are also shown, for values ranging from  $-0.02$  to  $-0.002$  in regions I and II and from  $-0.0002$  to  $-0.000002$  in regions III and IV.

not the distance to the centre  $C$  of the recirculation zone. In cylindrical geometry, the quantity  $\Delta(r_0)$  corresponds to the discriminant introduced by Rayleigh to distinguish centrifugally stable from unstable flows. Rayleigh's initial argument (Rayleigh 1916) was a necessary condition for instability, but Synge (1933) has proved that it is also a sufficient condition for centrifugal instability. Bayly (1988) generalized the latter argument to more general streamlines, i.e. convex streamlines where the square of the circulation decreases everywhere, and then Sipp & Jacquin (2000) obtained criterion (4.1).

Negative isocontours of the Rayleigh discriminant are represented in figure 6 where the separatrix linking the detachment point  $D$  to the reattachment point  $R$  and containing all the closed streamlines can be identified bordering the grey zone. Note that the aspect ratio is different from figures 1, 3 and 5. Circled points are drawn on the streamline depicted in figure 6, labelled  $i = 0, 2, \dots, 20$  such that the absolute time values at these points are  $t_i = i \times 100$  when following a particle on its trajectory. This gives an idea of the velocity intensity along the streamline. There exist different regions of the flow where the Rayleigh determinant is negative: a strong region (I) in the upstream and concave region of the bump, region (II) just preceding the detachment, weak regions (III) and (IV) in the recirculation zone and a last region (V) (not shown) downstream of the recirculation zone. There is no closed streamline along which the local Rayleigh discriminant remains negative and criterion (4.1) is not satisfied. However, particles following closed streamlines inside the recirculation zone pass every period through regions where they feel the centrifugal instability. Keeping in mind that (4.1) is only a sufficient condition for instability, the aim of § 4.2 is to analyse if this partial gain is sufficient to trigger the global instability revealed in § 3 by our global mode analysis. As noticed by Beaudoin *et al.* (2004) in the case of the backward facing step, the most unstable region upstream of the bump is naturally associated with a Görtler instability. However, the Görtler instability is a convective instability which is not observed in the 3D numerical simulations of § 2 in the absence of external noise, nor in global mode calculations of § 3.



4.2. WKB method along streamlines

In the so-called geometric optics method (or WKB method), the perturbation velocity and pressure are sought of the form

$$[\mathbf{u}, p] = [\mathbf{a}(t), \mathbf{b}(t)]e^{i\mathbf{k}(t)\cdot\mathbf{x}(t)}. \tag{4.3}$$

Following Bayly (1988), this enables one to evaluate a growth rate associated with any closed streamline in the limit of zero viscosity and large wavenumber  $\mathbf{k}$  by integrating the following set of equations:

$$\frac{d\mathbf{x}}{dt} = \mathbf{U}(\mathbf{x}(t)), \tag{4.4}$$

$$\frac{d\mathbf{k}}{dt} = -\mathbf{L}^T(\mathbf{x}(t))\mathbf{k}, \tag{4.5}$$

$$\frac{d\mathbf{a}}{dt} = \left( \frac{2\mathbf{k}(t)\mathbf{k}(t)^T}{|\mathbf{k}(t)|^2} - \mathbf{I} \right) \mathbf{L}(\mathbf{x}(t))\mathbf{a}, \tag{4.6}$$

where  $\mathbf{L}(\mathbf{x}(t))$  is the velocity-gradient matrix  $\nabla\mathbf{U}$  at position  $\mathbf{x}(t)$  attained at time  $t$ . The first equation simply restates that the (two-dimensional) position of the particle along the trajectory  $\mathbf{x}(t)$  remains tangent to the velocity vector  $\mathbf{U}(\mathbf{x}(t))$ . The second and third equations describe respectively the evolution of the three-dimensional wavenumber  $\mathbf{k}(t)$  and perturbation amplitude  $\mathbf{a}(t)$  along the streamline as time evolves. Three initial conditions should be added:

$$\mathbf{x}(t = 0) = \mathbf{x}_0, \quad \mathbf{k}(t = 0) = \mathbf{k}_0, \quad \mathbf{a}(t = 0) = \mathbf{a}_0, \tag{4.7}$$

where the first condition imposes the Lagrangian origin  $\mathbf{x}_0$  of the streamline and thereby entirely identifies the streamline.

Since the third column of  $\mathbf{L}$  and thereby the third line of  $\mathbf{L}^T$  are zero, the transverse component  $k_z = \beta$  of  $\mathbf{k}$  remains constant as time evolves. In contrast, the in-plane components evolve under the action of the deformation tensor. Bayly (1988), Sipp & Jacquin (1998) and Lifshitz & Hameiri (1991) have however shown that centrifugal and hyperbolic instabilities do attain their maximum growth rate for purely transverse wavenumbers, sometimes called *pressureless modes* (see also Leblanc & Godefert 1999; Godefert, Cambon & Leblanc 2001). In the light of the structures found in the previous sections by DNS and global mode analysis, we adopt the hypothesis  $\mathbf{k}_0 = \beta_0\mathbf{e}_z$  yielding  $\mathbf{k}(t) = \beta_0\mathbf{e}_z$ . With this assumption, (4.6) becomes

$$\frac{d\mathbf{a}}{dt} = \tilde{\mathbf{L}}(\mathbf{x}(t))\mathbf{a}, \tag{4.8}$$

where

$$\tilde{\mathbf{L}} = \begin{pmatrix} -1 & 0 & 0 \\ 0 & -1 & 0 \\ 0 & 0 & 1 \end{pmatrix} \mathbf{L}.$$

As a consequence of the periodic nature of the flow along closed streamlines, equation (4.8) is studied using Floquet theory over one period  $T(\mathbf{x}_0)$ :

$$\frac{d\mathbf{A}}{dt} = \tilde{\mathbf{L}}(\mathbf{x}(t))\mathbf{A} \quad \text{with} \quad \mathbf{A}(t = 0) = \mathbf{Id}. \tag{4.9}$$

The growth rate is then obtained by calculating the Floquet exponents associated with the eigenvalues  $\lambda_1(\mathbf{x}_0)$ ,  $\lambda_2(\mathbf{x}_0)$  and  $\lambda_3(\mathbf{x}_0)$  and associated eigenvectors  $\mathbf{a}_1(\mathbf{x}_0)$ ,  $\mathbf{a}_2(\mathbf{x}_0)$  and  $\mathbf{a}_3(\mathbf{x}_0)$  of the  $3 \times 3$  matrix  $\mathbf{A}(T(\mathbf{x}_0))$ . Equation (4.8) readily leads to  $\lambda_3 = 1$  and  $\mathbf{a}_3 = \mathbf{e}_z$

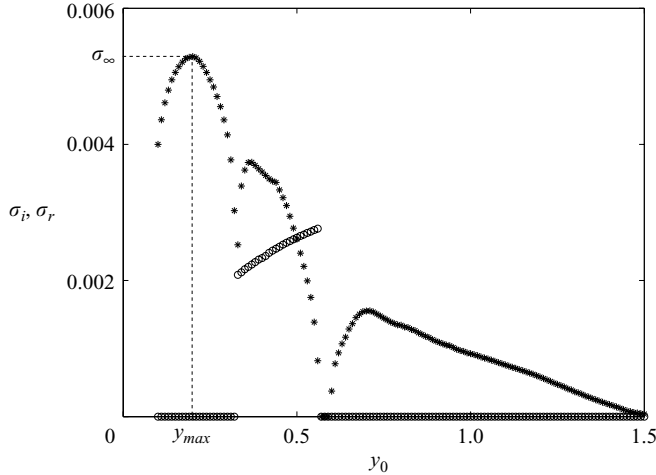


FIGURE 7. Growth rate (\*) and frequency (o) of the WKB mode as a function of the streamline labelled by the abscissa  $y_0$  along the segment represented in figure 6 as a dashed line.

and we further adopt the convention  $|\lambda_1| \geq |\lambda_2|$ . Since the trace of  $\mathbf{L}$  is always zero (and hence  $\text{Tr}(\tilde{\mathbf{L}}) = 0$ ) as a consequence of the divergence-free nature of the base flow, the determinant of  $\mathbf{A}(T)$  is unity ( $\det(\mathbf{A}(T)) = 1$ ) as a consequence of the Liouville theorem, yielding  $\lambda_2 = 1/\lambda_1$ . The maximum growth rate is then evaluated by considering the real part of

$$\sigma_1(\mathbf{x}_0) = \log(\lambda_1(\mathbf{x}_0))/T(\mathbf{x}_0). \quad (4.10)$$

Note that for any Lagrangian origin  $\mathbf{x}_0$  belonging to the streamline  $\psi_0$ ,  $\sigma_1(\mathbf{x}_0) \equiv \sigma_1(\psi_0)$ .

Equation (4.9) together with (4.4) are integrated via a fourth-order Runge–Kutta method for Lagrangian origins on several streamlines. The corresponding real and imaginary parts of  $\sigma_1(\psi_0)$  are reported in figure 7 where each streamline  $\psi_0$  is labelled by the ordinate  $y_0$  of the intersection point with the line depicted in figure 6 parallel to the  $y$ -axis from the center  $C = (62, 1.54)$  to the wall. As a complement, the intensity of the growth rate associated with each closed streamline is also reported in figure 6 using a grey scale. The maximum growth rate is stationary ( $\text{Im}(\sigma) = 0$ ), in agreement with the numerical simulation and global instability analysis and it is obtained for the streamline shown in figure 6 and corresponding to  $y_0 = y_{max} = 0.2$  in figure 7.

These results seem to indicate that the global net budget through centrifugally unstable ( $\Delta < 0$ ) and stable regions ( $\Delta > 0$ ) is positive. Since the stable regions have no damping property however ( $\sqrt{-\Delta}$  being purely imaginary), this simplified way of reasoning from a scalar viewpoint is clearly not relevant: it would lead to an erroneous sufficient criterion for instability requiring only that there exists some  $r_0$  belonging to the streamline  $\psi_0$  where  $\Delta(r_0) < 0$ . In reality the dynamics cannot be reduced to a scalar equation and the observed instability results from a detailed balance of transient growth and transient decrease periods, directly exploiting the time-dependent operator non-normality (see Farrell & Ioannou 1996, for details) ensured by the two degrees of freedom of the system.

#### 4.3. Towards a quantitative comparison

The previous subsection has clearly shown that the inviscid WKB analysis at large wavenumber enables one to detect a stationary instability which is in qualitative

agreement with the global mode analysis. In contrast, there is no quantitative agreement between the growth rate predicted in the large-wavenumber asymptotic limit  $\beta \rightarrow \infty$  and  $Re \rightarrow \infty$  ( $\sigma_\infty \sim 5 \times 10^{-3}$ ) and the growth rate measured in the global mode analysis at  $Re = 400$  and  $\beta = 0.3 = O(1)$  ( $\sigma \sim 8 \times 10^{-4}$ ). Note however that the reference length scale used to measure  $\beta$  is the displacement thickness, which is at least two orders of magnitude smaller than the streamline length representative of the physically relevant length scale. The effective wavenumber, once scaled with the streamline length, should therefore also be larger by two orders of magnitude giving some validity to our attempt to reach  $\beta = 0.3$  via the large-wavenumber asymptotic limit.

Landman & Saffman (1987) have discussed how to introduce a term accounting for the viscous time. Formally, equations similar to (4.4)–(4.6) starting from the Navier–Stokes and not the Euler equations can be derived. Equations (4.4) and (4.5) remain unchanged and equation (4.8) should be replaced by

$$\frac{da}{dt} = \left( \tilde{L} - \frac{\beta^2}{Re} \right) a, \tag{4.11}$$

which leads to the viscous corrected growth rate

$$\sigma_{vis} = \sigma_\infty - \frac{\beta^2}{Re}. \tag{4.12}$$

Bayly (1988) and Sipp & Jacquin (1998) have demonstrated that it is possible to build an inviscid global mode of finite wavenumber  $\beta$  in the vicinity of the most unstable streamline  $\psi_{max}$  if (4.1) holds. The rigorous derivation and asymptotic resolution of the boundary layer equations concentrated around  $\psi_{max}$  make explicit use of property (4.1) and reveal that the first-order correction term including finite- $\beta$  effects is a term of order  $-A/\beta$  accounting for the asymptotically small spreading of the unstable mode. A similar correction term can only be inferred here (as done for instance by Sipp, Lauga & Jacquin 1999, regarding hyperbolic and even elliptic instabilities) and enables one to suggest the following composite estimation:

$$\sigma = \sigma_\infty - \frac{\beta^2}{Re} - \frac{A}{\beta}, \tag{4.13}$$

which strictly makes sense only if  $ARe = O(\beta^3)$ . In this way of reasoning, one neglects the influence of the viscosity in the mode structure, i.e. one expects  $A$  not to depend on  $Re$ . Equation (4.13) may now be used to derive scaling laws for the maximum growth rate  $\sigma_{max}$  and wavenumber  $\beta_{max}$ :

$$\beta_{max} = \left( \frac{ARe}{2} \right)^{1/3} \tag{4.14}$$

$$\sigma_{max} = \sigma_\infty - (2^{1/3} + 2^{-2/3}) \left( \frac{A^2}{Re} \right)^{1/3}. \tag{4.15}$$

It is interesting to note that at  $\beta_{max}$ , the viscous correction and finite- $\beta$  terms are of the same order, guaranteeing that  $ReA = O(\beta^3)$ , thereby justifying the composite estimation (4.13).

The global mode stability analysis of §3 can be used to check this scaling law. This method is perfectly suited to decoupling the Reynolds number acting as the control parameter determining the steady base flow topology from the Reynolds number governing the perturbation evolution, as required in the above derivation. Three numerical experiments where the viscosity is changed in the stability equations (but not in the

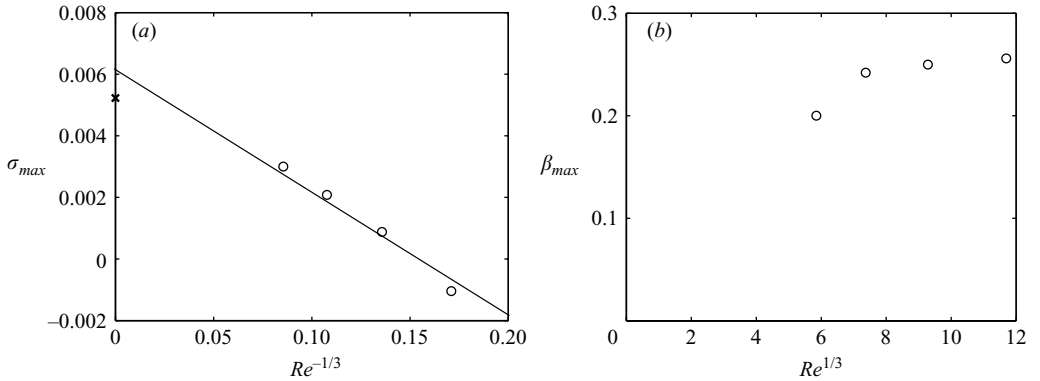


FIGURE 8. (a) Maximal growth rate  $\sigma_{max}$  ( $\circ$ ) as computed from the global stability analysis at various Reynolds numbers  $Re$  as a function of  $Re^{-1/3}$ . The inviscid asymptotic growth rate  $\sigma_{\infty}$  is also shown ( $\times$ ). (b) Wavenumber  $\beta_{max}$  ( $\circ$ ) at maximal growth rate as a function of  $Re^{1/3}$ .

base state) were conducted, at  $Re = 200$ ,  $Re = 800$  and  $Re = 1600$ , in a similar way to § 3. Higher Reynolds numbers showed unstable modes associated with the shear layer instability which were no longer localized in the recirculation zone. The corresponding maximal numerical growth rates are reported in figure 8(a) as a function of  $Re^{-1/3}$ . The four test cases fall on the same line  $\sigma = \sigma_0 - \sigma_1 Re^{-1/3}$  with  $\sigma_0 \sim 0.06$  close to  $\sigma_{\infty}$ . The quality of the collapse suggests that  $A$  does not depend on  $Re$ , giving some support to the hypothesis that viscous corrections in the construction of the eigenmode may be neglected. Note however that the scaling law (4.14) is not followed by  $\beta_{max}$  (figure 8b). We conclude that the geometric optics method designed for short long-wave inviscid instabilities, once suitably amended by viscous and finite wavenumber correction terms, hence provides a quantitatively correct estimate of the growth rate at the origin of the three-dimensional transverse instability taking place in the recirculation zone.

## 5. Conclusion

We have conducted a three-dimensional numerical study of a detached boundary layer over a bump at  $Re = 400$  and a global mode analysis based upon a two-dimensional base state. The comparison of the two stationary perturbed three-dimensional flow state structures is remarkable. In particular, it has been proved that no other instability mechanisms set in during the numerical simulation apart from those predicted by the global stability analysis. The local WKB analysis in the inviscid and short-wave limit shows that it is possible to identify closed streamlines along which the integrated growth rate is positive, although the particles cross inactive regions of the flow, as a consequence of a rather subtle parametric instability involving the periodic time evolution of the velocity-gradient tensor of the base flow along closed streamlines. This provides a reassessment of the inviscid nature of the present stationary longitudinal instability which has been suggested by Barkley *et al.* (2002) and Beaudoin *et al.* (2004), without however fully justifying its ‘centrifugal’ origins. A composite estimation of the growth rate taking into account the short-wave inviscid asymptotic limit as well as a viscous damping term and a finite wavenumber correction has been shown to compare favourably with the global mode analysis.

We would like to acknowledge P. Billant for stimulating discussions on the geometric optics technique. Both the three-dimensional DNS and the global mode computations have been performed on the IDRIS (Institute des Développement et des Ressources en Informatique Scientifique) NEC/SX5 under Grant 4055.

## REFERENCES

- ARMALY, B., DURST, F., PEREIRA, J. & SCHONUNG, B. 1983 Experimental and theoretical investigation of backward-facing step flow. *J. Fluid Mech.* **127**, 473–496.
- BARKLEY, D., GOMES, M. & HENDERSON, D. 2002 Three-dimensional instability in flow over a backward-facing step. *J. Fluid Mech.* **473**, 167–189.
- BAYLY, B. 1986 Three-dimensional instability of elliptical flow. *Phys. Rev. Lett.* **57**, 2160–2163.
- BAYLY, B. 1988 Three-dimensional centrifugal type instability in an inviscid two-dimensional flow. *Phys. Fluids* **31**, 56–64.
- BEAUDOIN, J.-F., CADOT, O., AIDER, J.-L. & WESFREID, J. 2004 Three-dimensional stationary flow over a backward-facing step. *Eur. J. Mech. B/Fluids* **23**, 147–155.
- EHRENSTEIN, U. & GALLAIRE, F. 2005 On two-dimensional temporal modes in spatially evolving open flows: the flat-plate boundary layer. *J. Fluid Mech.* **536**, 209–218.
- FARRELL, B. & IOANNOU, P. J. 1996 Generalized stability theory part ii: non-autonomous operators. *J. Atmos. Sci.* **53**, 2041–2053.
- GODEFERD, F., CAMBON, C. & LEBLANC, S. 2001 Zonal approach to centrifugal, elliptic and hyperbolic instabilities in Stuart vortices with system rotation. *J. Fluid Mech.* **449**, 1–37.
- HAMMOND, D. & REDEKOPP, L. 1998 Local and global instability properties of separation bubbles. *Eur. J. Mech. B/Fluids* **17**, 145–164.
- KAIKTSIS, L., KARNIADAKIS, G. & ORSZAG, S. 1991 Onset of three-dimensionality equilibria and early transition in flow over a backward-facing step. *J. Fluid Mech.* **231**, 501–528.
- KAIKTSIS, L., KARNIADAKIS, G. & ORSZAG, S. 1996 Unsteadiness and convective instabilities in two-dimensional flow over a backward facing step. *Eur. J. Mech. B/Fluids* **321**, 157–187.
- LANDMAN, M. J. & SAFFMAN, P. 1987 The three-dimensional instability of strained vortices in a viscous fluid. *Phys. Fluids* **30**, 2339–2342.
- LEBLANC, S. & GODEFERD, F. S. 1999 An illustration of the link between ribs and hyperbolic instability. *Phys. Fluids* **11**, 497–499.
- LIFSHITZ, A. & HAMEIRI, E. 1991 Local stability conditions in fluid dynamics. *Phys. Fluids A* **3**, 2644–2651.
- MARQUILLIE, M. & EHRENSTEIN, U. 2002 Numerical simulation of separating boundary-layer flow. *Computers Fluids* **31**, 683–693.
- MARQUILLIE, M. & EHRENSTEIN, U. 2003 On the onset of nonlinear oscillations in a separating boundary-layer flow. *J. Fluid Mech.* **490**, 169–188.
- RAYLEIGH, LORD 1916 On the dynamics of revolving fluids. *Proc. R. Soc. Lond. A* **93**, 148–154.
- SIPP, D. & JACQUIN, L. 1998 Elliptic instability in two-dimensional flattened Taylor-Green vortices. *Phys. Fluids* **10**, 839–849.
- SIPP, D. & JACQUIN, L. 2000 Three-dimensional centrifugal-type instabilities of two-dimensional flows in rotating systems. *Phys. Fluids* **12**, 1740–1748.
- SIPP, D., LAUGA, E. & JACQUIN, L. 1999 Vortices in rotating systems: centrifugal, elliptic and hyperbolic type instabilities. *Phys. Fluids* **11**, 3716–3728.
- SYNGE, J. L. 1933 The stability of heterogeneous liquids. *Trans. R. Soc. Canada* **27**, 1–18.
- THEOFILIS, V., HEIN, S. & DALLMANN, U. 2000 On the origins of unsteadiness and three-dimensionality in a laminar separation bubble. *Phil. Trans. R. Soc. Lond. A* **358**, 3229–3246.
- WILLIAMS, P. & BAKER, A. 1997 Numerical simulations of laminar flow over a 3D backward facing step. *Intl J. Numer. Meth. Fluids* **24**, 1159–1183.